

The deep blue color of HD 189733b: albedo measurements with *HST*/STIS at visible wavelengths

T. M. Evans¹, F. Pont², D. K. Sing², S. Aigrain¹, J. K. Barstow¹, J.-M. Désert^{5,7},
N. Gibson⁴, K. Heng³, H. A. Knutson⁵, A. Lecavelier des Etangs⁶

ABSTRACT

We present a secondary eclipse observation for the hot Jupiter HD 189733b across the wavelength range 290–570 nm made using the Space Telescope Imaging Spectrograph on the Hubble Space Telescope. We measure geometric albedos of $A_g = 0.40 \pm 0.12$ at 290–450 nm and $A_g < 0.12$ at 450–570 nm. The albedo decrease towards longer wavelengths is also apparent when using six wavelength bins over the same wavelength range. This can be interpreted as evidence for optically thick reflective clouds on the dayside hemisphere, with sodium absorption suppressing the scattered light signal beyond ~ 450 nm as predicted by models of hot Jupiter atmospheres. Our best-fit albedo values imply that HD 189733b would appear a deep blue color at visible wavelengths.

Subject headings: planets and satellites: atmospheres - stars: individual (HD 189733)
- techniques: photometric

1. Introduction

The wavelength-dependent manner in which a planetary atmosphere reflects incident starlight reveals valuable details about its structure and composition. In this Letter, we

¹ Department of Physics, University of Oxford, Denys Wilkinson Building, Keble Road, Oxford OX1 3RH, UK

² School of Physics, University of Exeter, EX4 4QL Exeter, UK

³ University of Bern, Center for Space and Habitability, Sidlerstrasse 5, CH-3012 Bern, Switzerland

⁴ European Southern Observatory, Karl-Schwarzschild-Strasse 2, D-85748 Garching, Germany

⁵ Division of Geological and Planetary Sciences, California Institute of Technology, Pasadena, CA 91125, USA

⁶ Institut d'Astrophysique de Paris, UMR7095 CNRS, Université Pierre et Marie Curie, 98 bis Boulevard Arago, F-75014 Paris, France

⁷ Sagan Postdoctoral Fellow

present albedo measurements for the transiting hot Jupiter HD 189733b across the wavelength range $\lambda = 290\text{--}570$ nm.

At these wavelengths, clear atmosphere models (i.e. without clouds) predict that reflection is suppressed due to absorption by saturated alkali wings, particularly the Na 589 nm doublet (Sudarsky et al. 2000; Burrows et al. 2008). Observations to date have been largely consistent with these expectations (e.g. Rowe et al. 2008; Alonso et al. 2009; Snellen et al. 2009; Alonso et al. 2010; Snellen et al. 2010; Christiansen et al. 2010; Welsh et al. 2010; Désert et al. 2011; Morris et al. 2013). Models also predict, however, that silicates and iron could condense in the uppermost layers of some hot Jupiter atmospheres, raising the albedo significantly (Marley et al. 1999; Sudarsky et al. 2000). For instance, reflective clouds seem necessary to explain the relatively high albedo of Kepler-7b (Kipping & Bakos 2011; Demory et al. 2011).

By measuring the reflection signal of HD 189733b, our goal was to gauge the role of clouds in the atmosphere of this particularly well-studied hot Jupiter. Motivation came from the atmospheric transmission spectrum, which slopes downwards from 290 nm out to at least $1\ \mu\text{m}$ (Pont et al. 2008; Sing et al. 2011) and possibly into the infrared (Sing et al. 2009; Gibson et al. 2012a). A likely explanation for this feature is Rayleigh scattering by a high altitude cloud of dust (Lecavelier Des Etangs et al. 2008; Pont et al. 2013), which could produce a high albedo at visible wavelengths. Further evidence for a dusty atmosphere has come from Huitson et al. (2012) who detected the narrow core of the Na 589 nm doublet in transmission, but not the pressure-broadened wings that would be expected in a clear atmosphere (e.g. Fortney et al. 2010).

In practice, we measured the reflection signal of HD 189733b by monitoring the change in brightness of the star-planet system that occurred during secondary eclipse. Unlike the primary transit, which allows us to probe the day-night terminator region of the atmosphere, the secondary eclipse signal is directly related to the brightness of the dayside hemisphere. Although secondary eclipses have been measured previously for HD 189733b at infrared wavelengths (Deming et al. 2006; Knutson et al. 2007; Grillmair et al. 2008; Charbonneau et al. 2008; Agol et al. 2010; Knutson et al. 2012), our new observation constitutes the first secondary eclipse that has been measured for HD 189733b at short wavelengths, where thermal emission from the planet is negligible. Any detected light is therefore entirely due to scattering by the atmosphere. This allows us to place unambiguous constraints on the geometric albedo A_g , according to:

$$A_g = \delta \left[\rho \frac{R_\star}{a} \right]^{-2}, \quad (1)$$

where δ is the fractional eclipse depth, $\rho = R_p/R_\star$ is the ratio of the planet and star radii,

and a is the orbital semimajor axis. Equation 1 follows from the formal definition of A_g , namely, the observed flux of the planet due to scattered light at full phase divided by the flux that an isotropically scattering disk with the same cross-sectional area would have if it were placed at the same location as the planet (e.g. see Seager 2010). Other types of albedo - such as the Bond albedo A_B , defined as the fraction of incident starlight reflected to space at all wavelengths over all angles - are not amenable to direct measurement.

The paper is arranged as follows: observations and data reduction are described in Section 2; the lightcurve modelling methodology is explained in Section 3; albedo results are presented in Section 4; and possible implications for the atmosphere of HD 189733b are discussed in Section 5.

2. Observations and data reduction

One secondary eclipse of HD 189733b was observed over four Hubble Space Telescope (*HST*) orbits using the Space Telescope Imaging Spectrograph (STIS) G430L grating (290–570 nm) for programme GO-13006 (P.I., F. Pont) on 2012 December 20. Spectra taken during the first orbit exhibited much larger systematics than those taken in subsequent orbits due to settling of the telescope into its new pointing position and were not included in the analysis. Of the remaining three orbits, the first and third sampled the out-of-eclipse flux while the planet was close to full phase (star plus planet), and the second sampled the in-eclipse flux while the planet was fully obscured by the star (star only).

We used a wide $52'' \times 2''$ slit to minimise time-varying slit losses caused by pointing drifts and reduced overheads by reading out only the 1024×128 pixel subarray containing the target spectrum. Based on previous experience with STIS observations, we expected the first exposure of each satellite orbit to have systematically lower counts than the exposures immediately following. For this reason, a dummy 1 s exposure was taken at the beginning of each orbit, followed by a series of 35 science exposures with integration times of 64 s. Unfortunately, the first science exposure of each satellite orbit still exhibited systematically lower flux levels, so we discarded these as well, leaving us with 34 science images per satellite orbit. Our final dataset thus consisted of 102 spectra taken over 237 mins.

Images were reduced using the CALSTIS v2.39 pipeline and cleaned for cosmic rays. The spectra were then extracted using the IRAF `apa11` routine with a 13 pixel-wide aperture. Background subtraction was not performed, as the background contribution was negligible. Spectra were Doppler-corrected to the heliocentric rest frame, corresponding to shifts of ~ 1 pixel along the dispersion axis. We generated photometric time series by integrating the

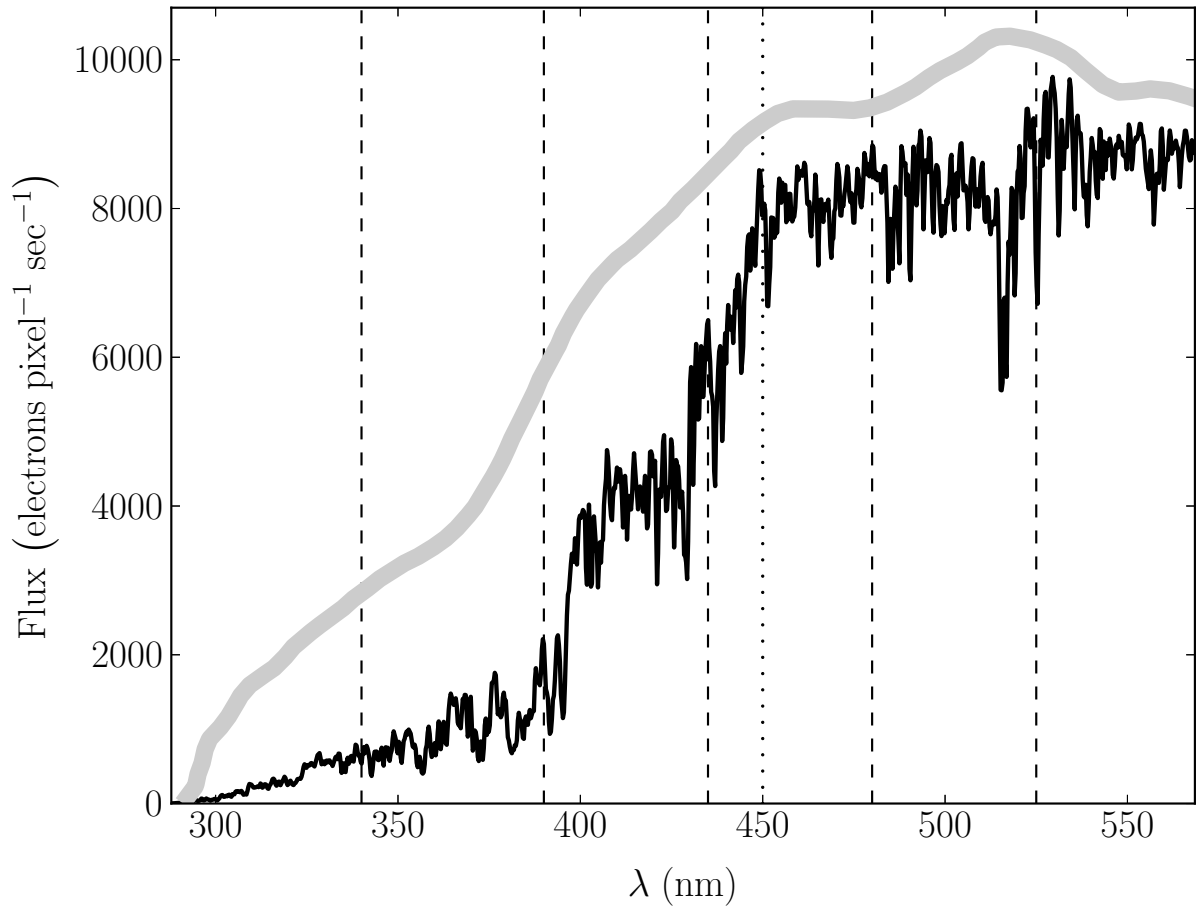


Fig. 1.— Mean stellar spectrum constructed from the out-of-eclipse spectra (solid black line), and G430L sensitivity curve with arbitrary normalization (thick gray line). Vertical lines indicate boundaries between the two-channel (dotted line) and six-channel (dashed lines) wavelength bins used for the lightcurve analysis.

flux from each individual exposure across the dispersion axis within different wavelength bins. Separate analyses were performed for a two-channel and six-channel binning: Figure 1 shows the mean stellar spectrum with the adopted wavelength bins overplotted and Table 1 explicitly lists the wavelength ranges.

3. Lightcurve analysis

The top panels of Figure 2 show the raw lightcurves for the two-channel binning. Within each orbit, the measured flux is dominated by an approximately repeatable decrease of ~ 2500 ppm. Smaller amplitude correlations on shorter time scales are also evident, as well as a longer term decrease in the baseline flux level. Similar systematics are observed for the six-channel lightcurves, and are believed to be primarily caused by the thermal cycle of the satellite and the drift of the spectral trace across the detector (eg. Brown et al. 2001; Sing et al. 2011; Huitson et al. 2012).

We modelled the systematics and eclipse signal simultaneously as a Gaussian process (GP), following the approach of Gibson et al. (2012a,b, 2013). Under the GP framework, the model likelihood takes the form of a multivariate normal distribution:

$$p(\mathbf{f}|\boldsymbol{\theta}) = \mathcal{N}(\boldsymbol{\mu}, \mathbf{K} + \sigma_W^2 \mathbf{I}) , \quad (2)$$

where $\mathbf{f} = [f_1, \dots, f_N]^T$ are the $N = 102$ measured fluxes, $\boldsymbol{\theta}$ are the model parameters, $\boldsymbol{\mu}$ is the model mean vector, \mathbf{K} is the covariance matrix, σ_W is the white noise level, and \mathbf{I} is the identity matrix. A boxcar function was used for the eclipse signal, such that:

$$\mu_i = \alpha (1 - \delta B_i) , \quad (3)$$

where α is the constant baseline flux level, δ is the fractional flux change during eclipse, and:

$$B_i = \begin{cases} 0 & \text{during 1st and 3rd orbits} \\ 1 & \text{during 2nd orbit} , \end{cases} \quad (4)$$

for $i = 1, \dots, N$.

Off-diagonal entries of the covariance matrix \mathbf{K} accounted for correlations between the measured flux and other variables that are unrelated to the eclipse signal, which we refer to as auxiliary variables (see below). We used the squared exponential kernel to populate the entries of \mathbf{K} , such that:

$$K_{ij} = C^2 \exp \left[- \sum_{d=1}^D \left(\frac{v_{d,i} - v_{d,j}}{L_d} \right)^2 \right] , \quad (5)$$

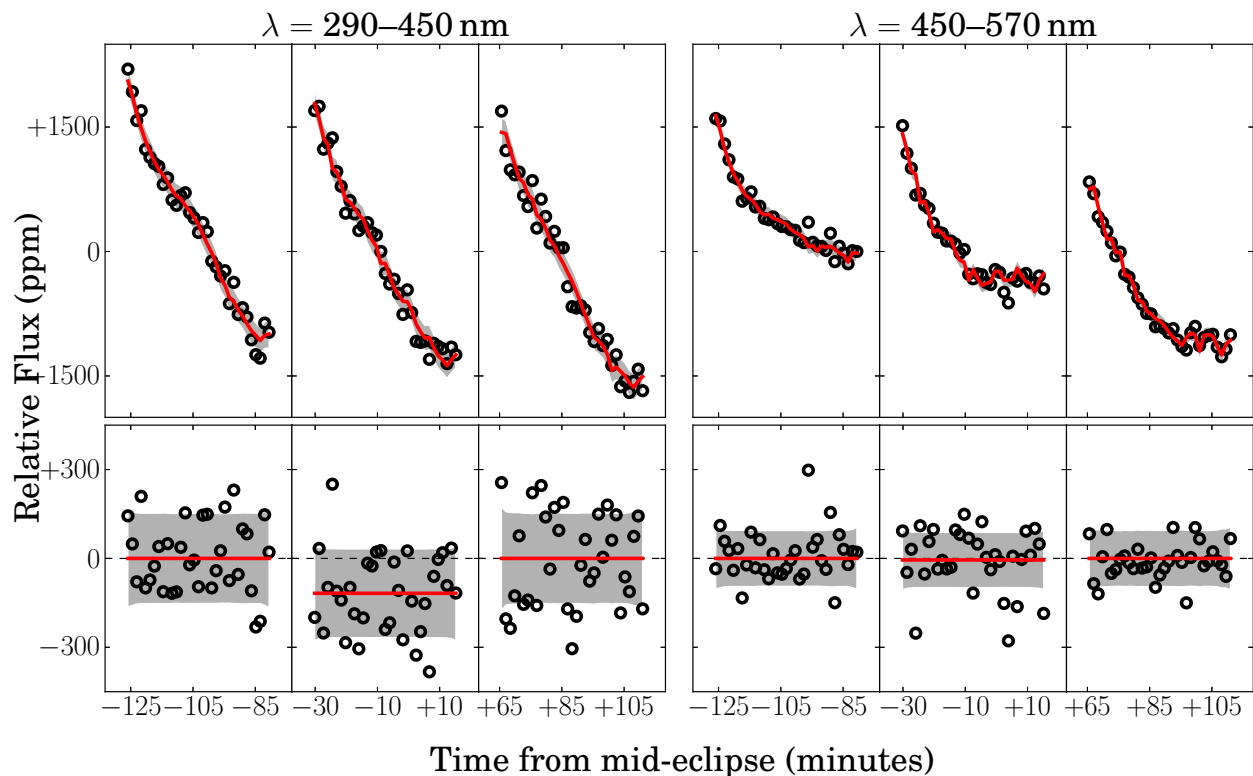


Fig. 2.— Top and bottom panels show, respectively, the raw and corrected flux measurements (black circles) with best-fit GP model (red lines) and per-point 1σ uncertainties (gray shading). The 290–450 nm and 450–570 nm wavelength channels are shown on the left and right, respectively. Raw fluxes have been median-subtracted and corrected fluxes show the variation about the out-of-eclipse baseline level.

where C^2 is the covariance amplitude, $v_{d,i}$ and $v_{d,j}$ are the i th and j th values of the d th auxiliary variable, respectively, and L_d is the correlation length scale of the d th auxiliary variable. By parameterizing the covariance according to Equation 5, we effectively model the poorly understood systematics as varying smoothly with respect to the auxiliary variables without actually having to specify the functional form. See Gibson et al. (2012b) for more details.

For auxiliary variables, we used the orbital phase of the satellite ϕ and the tilt of the spectral trace on the detector ψ . The ϕ -dependence accounted for the dominant systematic that repeated from orbit-to-orbit, while the ψ -dependence accounted for the smaller amplitude, higher frequency correlations as well as the longer-term decrease in the flux baseline level (Figure 2). The latter was due to an overall drift in the value of ψ throughout the observations, in addition to a lower-amplitude jitter within orbits. We also tried including the measured shifts of the spectral trace along the dispersion x -axis and cross-dispersion y -axis as additional auxiliary variables, but found their inclusion had a negligible effect on the result. Our final parameter set therefore consisted of $\boldsymbol{\theta} = \{ \delta, \alpha, C, L_\phi, L_\psi, \sigma_W \}$.

To marginalize Equation 2 over the space spanned by $\boldsymbol{\theta}$, we used the open source software package PyMC (Patil et al. 2010) to implement Markov Chain Monte Carlo (MCMC) sampling with the Metropolis-Hastings algorithm (Metropolis et al. 1953; Hastings 1970). We ran five chains of 120,000 steps each, where a single step consisted of cycling through the parameters and updating their values one at a time. Random step sizes were adjusted separately for each parameter to maintain step acceptance rates of 20–40% throughout the chains. After discarding the first 20,000 steps as burn-in, we thinned the remaining chain segments by a factor of 10 to reduce correlations between neighbouring steps. Gelman-Rubin values (Gelman & Rubin 1992) were found to be well within 1% for all parameters, suggesting that the chains had converged and were well-mixed. The five separate chains were then combined to give a single chain of 50,000 samples.

As a check, we also modelled the systematics with different linear combinations of the auxiliary variables, and using the Bayesian information criterion (BIC) to choose between models. This has become the standard approach for analyzing STIS datasets for transit lightcurves (e.g. Sing et al. 2011; Huitson et al. 2012). The eclipse depths inferred from these analyses were consistent with those obtained using the GP model, verifying the robustness of the results to the treatment of instrumental systematics.

4. Results

Best-fit GP models for the two-channel binning are shown as red lines in Figure 2, with gray regions indicating 1σ uncertainties. Inferred eclipse depths δ are reported in Table 1 for all wavelength channels. The median of the combined MCMC chain is quoted with uncertainties that correspond to ranges either side containing 34% of the samples. Maximum likelihood estimate values were also obtained for each parameter using the Nelder-Mead simplex algorithm (Nelder & Mead 1965) to optimize the joint GP likelihood given by Equation 2 with respect to θ , taking the median MCMC chain values as starting points. In all cases, the binned chain values for δ had Gaussian-like distributions, and the maximum likelihood solutions were very close to the median chain values.

Table 1 also lists the values for the geometric albedo A_g , calculated using Equation 1 with the measured δ values, $\rho = 0.157 \pm 0.001$ (Pont et al. 2013), and $a/R_\star = 8.863 \pm 0.020$ (Agol et al. 2010). The most striking result is that the measured albedo in the wavelength range 290–450 nm ($A_g = 0.40 \pm 0.12$) is significantly higher than it is in the wavelength range 450–570 nm ($A_g < 0.12$). The broad trend of decreasing eclipse depth from shorter to longer wavelengths is also recovered from the six-channel analysis.

4.1. Stellar variability

In this section, we address the possibility that variations in the brightness of the star itself, rather than the planetary eclipse, could be responsible for the measured signal. This is particularly pertinent for HD 189733, which is known to be an active K dwarf.

Using 5000K and 4200K NextGen stellar models (Hauschildt et al. 1999) for the star and spot spectrum, respectively, with solar metallicity and $\log_{10} g = -4.5$, we find the flux drop in the 290–450 nm channel would only be $\sim 10\%$ greater than the flux drop in the 450–570 nm channel. The measured difference is significantly larger than this.

We can also estimate the characteristic amplitude of flux variations due to stellar activity using the power law index of -2.3 obtained by McQuillan et al. (2012) for the combined power spectrum of the brightest K dwarfs in the Q1 *Kepler* dataset. Scaling this to the $\sim 1\%$ variation amplitude over ~ 10 day timescales for HD 189733, we obtain a corresponding amplitude of ~ 30 ppm in the 290–450 nm channel on timescales of 90 minutes (i.e. *HST* orbital period). This is less than half the flux change observed and slightly smaller than the uncertainty on δ due to other sources.

Table 1. Visible albedo measurements for HD 189733b

$\Delta\lambda$ (nm)	λ_c (nm)	δ (ppm)	A_g
290–450	413	126^{+37}_{-36}	$0.40^{+0.12}_{-0.11}$
450–570	510	1^{+37}_{-30}	$0.00^{+0.12}_{-0.10}$
290–340	325	142^{+176}_{-175}	$0.45^{+0.55}_{-0.55}$
340–390	368	123^{+86}_{-87}	$0.39^{+0.27}_{-0.27}$
390–435	416	102^{+48}_{-48}	$0.32^{+0.15}_{-0.15}$
435–480	459	53^{+37}_{-36}	$0.17^{+0.12}_{-0.11}$
480–525	502	-35^{+45}_{-36}	$-0.11^{+0.14}_{-0.11}$
525–570	547	7^{+43}_{-36}	$0.02^{+0.14}_{-0.12}$

Note. — $\Delta\lambda$ and λ_c are, respectively, the wavelength range and flux-weighted central wavelength for each channel.

5. Implications for the atmosphere

To first order, the reflection spectrum of a hot Jupiter at visible wavelengths will depend on whether or not there is a layer of reflective clouds in the atmosphere, and the altitude at which it becomes optically thick (e.g. Sudarsky et al. 2000). Explicitly, we can identify three broad scenarios on a continuum of possibilities: if scattering clouds are present and become optically thick at pressures below the absorption wings of the Na 589 nm doublet and other atomic and molecular absorbers, high albedos ($A_g \sim 0.4\text{--}0.6$) can be maintained throughout the visible wavelength range (e.g. Class V models of Sudarsky et al. 2000). If there are no clouds, or clouds are present but become optically thick at altitudes well below the absorption, then the albedo can be much lower. Expected values at visible wavelengths in this case will be $A_g < 0.2$ (e.g. “irradiated” Class IV models of Sudarsky et al. 2000). In intermediate cases, if clouds are present and become optically thick at pressures comparable to the Na absorption wings, the albedo can be high in the blue channel relative to the red channel¹ (e.g. “isolated” Class IV models of Sudarsky et al. 2000).

This list is by no means exhaustive - additional complicating factors could include the possible depletion of Na or the presence of condensates that absorb, rather than scatter, incident light. However, we currently have no reason to suspect that these apply to HD 189733b, and given the modest resolution and precision of our measurements, we restrict our discussion to the three cases listed above.

The significantly higher albedo that we measure in the blue channel compared to the red channel rules out the first and second scenarios, but is compatible with the third. To investigate this possibility further, we developed a simple toy model to estimate the expected reflection signal. First, we took the photon deposition pressure as a function of wavelength from the HD 189733b model of Fortney et al. (2008) and assumed that this pressure is inversely proportional to the absorption opacity in the atmosphere. Second, we added a population of grains that scatter incoming starlight with a Rayleigh λ^{-4} dependence, varying the pressures levels at which this population becomes optically thick to simulate clouds with different optical depths and altitudes. Third, with the absorption and scattering properties of the atmosphere as a function of wavelength now defined, we calculated the albedo according to the two-stream approximation of Heng et al. (2012), given as: $A_g = \frac{3}{4}(1 - \xi^{1/2})/(1 + \xi^{1/2})$, where ξ is the ratio of absorption to total opacity (absorption+scattering) in a given passband. We vary the height of the clouds in steps of two atmospheric pressure scale heights, from a high level covering the wings of the sodium doublet, to a low level close

¹In the following discussion, we refer to the 290–450nm and 450–570nm ranges as the blue and red channels, respectively.

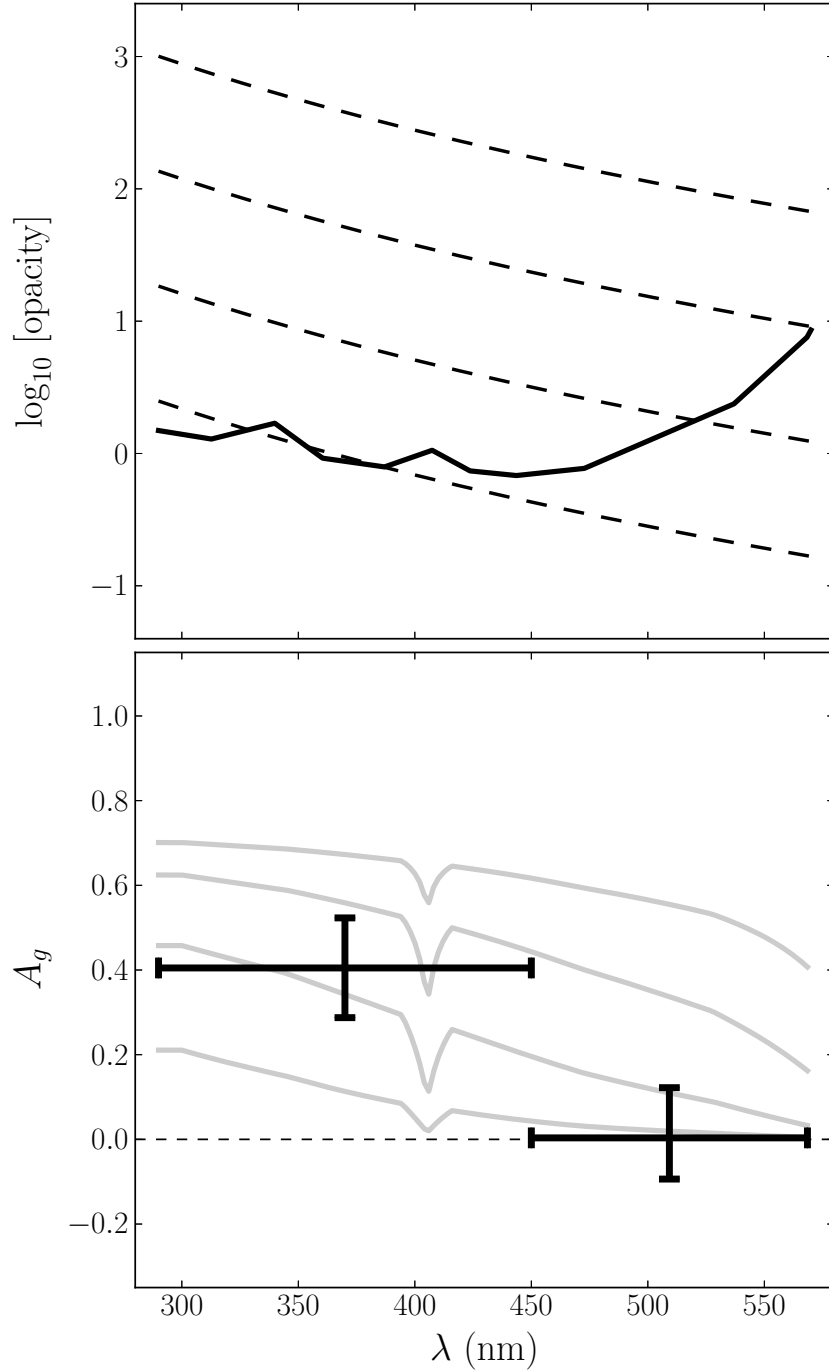


Fig. 3.— *Top panel*: Relative contributions of absorption and scattering to the total opacity in our toy model. Solid line shows atomic and molecular absorption. Dashed lines indicate Rayleigh scattering due to clouds that become optically thick at different altitudes, separated by increments of two atmospheric scale heights. Opacity units are arbitrary because they cancel out when the albedo is calculated according to our toy model, which is described in the text. *Bottom panel*: Black crosses show measured geometric albedos for the two-channel analysis, with vertical bars indicating 1σ uncertainties and horizontal bars indicating the extent of the corresponding wavelength channels. Gray lines show toy model predictions for the different cloud altitudes shown in the top panel.

to the expected level of Rayleigh scattering by H_2 molecules. The top panel of Figure 3 shows the adopted opacity profiles, with scattering and absorption contributions identified separately, and the bottom panel shows the resulting albedo spectra, with our measured values overplotted. The model with clouds becoming optically thick four scale heights below the peak of the Na doublet provides a reasonable fit to the observations.

An interesting question is whether or not the reflection signal is caused by the same scattering species that produces the Rayleigh profile in the transmission spectrum. Given the strong atmospheric circulation expected for hot Jupiters, this would be plausible (e.g. Showman et al. 2009; Perna et al. 2012). Lecavelier Des Etangs et al. (2008) identified enstatite grains (MgSiO_3) as likely candidates, being transparent in the visible and formed of atoms abundant in hot atmospheres.

The limited precision of the current data prevents us from ruling out more intricate scenarios. For example, a high altitude tenuous haze could account for the transmission signal while being transparent at zenith geometry, with a lower, denser layer of clouds producing the reflection signal. The absorption in the red channel could also be due to an absorber other than Na, yet to be identified. Titanium oxide, for instance, is an efficient absorber in the red channel, although it is expected to have rained out of the atmosphere of HD 189733b (Fortney et al. 2008).

We note that we are not the first to claim that the albedo of HD 189733b decreases across the visible wavelength range. Berdyugina et al. (2008, 2011) reported albedos of $A_g = 0.61 \pm 0.12$ and $A_g = 0.28 \pm 0.16$ in the *B* (390–480 nm) and *V* (500–590 nm) bands, respectively, inferred from polarization data. Our results are systematically lower than these values, but compatible at the $\sim 2\sigma$ level.

If the low albedo we measure in the red channel persists at longer wavelengths, HD 189733b would reflect minimal light in the *Kepler* passband (400–900 nm). This would put it amongst majority of hot Jupiters with albedos constrained by *Kepler* to date. It would also imply that absorption is more important than scattering at wavelengths where most of the starlight is emitted, providing some justification for the standard assumption in circulation models that the Bond albedo is close to zero.

Finally, in Figure 4 we show the blue-versus-red albedos for HD 189733b and a selection of solar system bodies that also have thick atmospheres, as well as predicted albedos from three hot Jupiter models. Berdyugina et al. (2011) hypothesize that HD 189733b might have a reflection spectrum similar to Neptune. However, our best-fit albedos suggest that it is a deep dark blue, quite distinct from the atmosphere colors seen in our solar system.

The results presented here demonstrate the potential of secondary eclipse observations

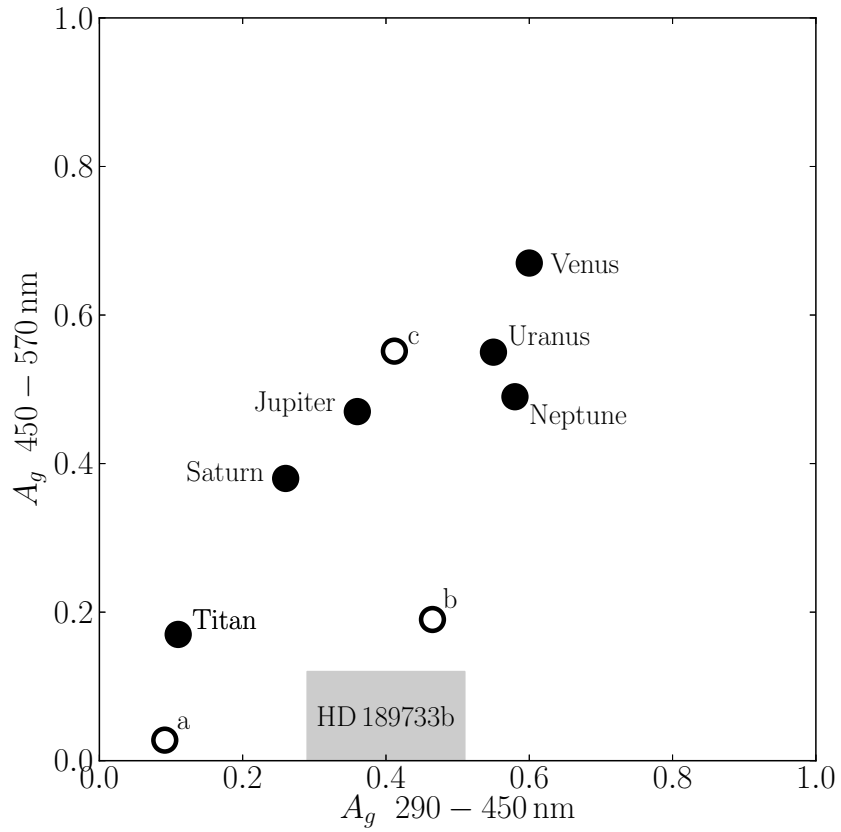


Fig. 4.— Color-color plot showing geometric albedos for various solar system bodies as black circles with the 1σ probability range for HD 189733b derived in this study. Solar system albedos have been taken from Karkoschka (1994). Open circles show three models from Sudarsky et al. (2000): (a) irradiated Class IV, (b) isolated Class IV, and (c) Class V.

with *HST*/STIS. Our albedo measurements add another piece to the growing jigsaw puzzle of empirical constraints on HD 189733b’s atmosphere, through which we are gradually moving towards a more complete understanding of this exotic planet.

REFERENCES

- Agol, E., Cowan, N. B., Knutson, H. A., Deming, D., Steffen, J. H., Henry, G. W., & Charbonneau, D. 2010, *ApJ*, 721, 1861
- Alonso, R., Alapini, A., Aigrain, S., Auvergne, M., Baglin, A., Barbieri, M., Barge, P., Bonomo, A. S., Bordé, P., Bouchy, F., Chaintreuil, S., de La Reza, R., Deeg, H. J., Deleuil, M., Dvorak, R., Erikson, A., Fridlund, M., de Oliveira Fialho, F., Gondoin, P., Guillot, T., Hatzes, A., Jorda, L., Lammer, H., Léger, A., Llebaria, A., Magain, P., Mazeh, T., Moutou, C., Ollivier, M., Pätzold, M., Pont, F., Queloz, D., Rauer, H., Rouan, D., Schneider, J., & Wuchterl, G. 2009, *A&A*, 506, 353
- Alonso, R., Deeg, H. J., Kabath, P., & Rabus, M. 2010, *AJ*, 139, 1481
- Berdyugina, S. V., Berdyugin, A. V., Fluri, D. M., & Piirola, V. 2008, *ApJ*, 673, L83
- . 2011, *ApJ*, 728, L6
- Brown, T. M., Charbonneau, D., Gilliland, R. L., Noyes, R. W., & Burrows, A. 2001, *ApJ*, 552, 699
- Burrows, A., Ibgui, L., & Hubeny, I. 2008, *ApJ*, 682, 1277
- Charbonneau, D., Knutson, H. A., Barman, T., Allen, L. E., Mayor, M., Megeath, S. T., Queloz, D., & Udry, S. 2008, *ApJ*, 686, 1341
- Christiansen, J. L., Ballard, S., Charbonneau, D., Madhusudhan, N., Seager, S., Holman, M. J., Wellnitz, D. D., Deming, D., A’Hearn, M. F., & EPOXI Team. 2010, *ApJ*, 710, 97
- Deming, D., Harrington, J., Seager, S., & Richardson, L. J. 2006, *ApJ*, 644, 560
- Demory, B.-O., Seager, S., Madhusudhan, N., Kjeldsen, H., Christensen-Dalsgaard, J., Gillon, M., Rowe, J. F., Welsh, W. F., Adams, E. R., Dupree, A., McCarthy, D., Kulesa, C., Borucki, W. J., & Koch, D. G. 2011, *ApJ*, 735, L12

- Désert, J.-M., Charbonneau, D., Fortney, J. J., Madhusudhan, N., Knutson, H. A., Fressin, F., Deming, D., Borucki, W. J., Brown, T. M., Caldwell, D., Ford, E. B., Gilliland, R. L., Latham, D. W., Marcy, G. W., & Seager, S. 2011, *ApJS*, 197, 11
- Fortney, J. J., Lodders, K., Marley, M. S., & Freedman, R. S. 2008, *ApJ*, 678, 1419
- Fortney, J. J., Shabram, M., Showman, A. P., Lian, Y., Freedman, R. S., Marley, M. S., & Lewis, N. K. 2010, *ApJ*, 709, 1396
- Gelman, A. & Rubin, D. B. 1992, *Stat. Sci.*, 7, 457
- Gibson, N. P., Aigrain, S., Barstow, J. K., Evans, T. M., Fletcher, L. N., & Irwin, P. G. J. 2013, *MNRAS*, 428, 3680
- Gibson, N. P., Aigrain, S., Pont, F., Sing, D. K., Désert, J.-M., Evans, T. M., Henry, G., Husnoo, N., & Knutson, H. 2012a, *MNRAS*, 422, 753
- Gibson, N. P., Aigrain, S., Roberts, S., Evans, T. M., Osborne, M., & Pont, F. 2012b, *MNRAS*, 419, 2683
- Grillmair, C. J., Burrows, A., Charbonneau, D., Armus, L., Stauffer, J., Meadows, V., van Cleve, J., von Braun, K., & Levine, D. 2008, *Nature*, 456, 767
- Hastings, W. K. 1970, *Biometrika*, 57, 97
- Hauschildt, P. H., Allard, F., & Baron, E. 1999, *ApJ*, 512, 377
- Heng, K., Hayek, W., Pont, F., & Sing, D. K. 2012, *MNRAS*, 420, 20
- Huitson, C. M., Sing, D. K., Vidal-Madjar, A., Ballester, G. E., Lecavelier des Etangs, A., Désert, J.-M., & Pont, F. 2012, *MNRAS*, 422, 2477
- Karkoschka, E. 1994, *Icarus*, 111, 174
- Kipping, D. & Bakos, G. 2011, *ApJ*, 730, 50
- Knutson, H. A., Charbonneau, D., Allen, L. E., Fortney, J. J., Agol, E., Cowan, N. B., Showman, A. P., Cooper, C. S., & Megeath, S. T. 2007, *Nature*, 447, 183
- Knutson, H. A., Lewis, N., Fortney, J. J., Burrows, A., Showman, A. P., Cowan, N. B., Agol, E., Aigrain, S., Charbonneau, D., Deming, D., Désert, J.-M., Henry, G. W., Langton, J., & Laughlin, G. 2012, *ApJ*, 754, 22
- Lecavelier Des Etangs, A., Pont, F., Vidal-Madjar, A., & Sing, D. 2008, *A&A*, 481, L83

- Marley, M. S., Gelino, C., Stephens, D., Lunine, J. I., & Freedman, R. 1999, *ApJ*, 513, 879
- McQuillan, A., Aigrain, S., & Roberts, S. 2012, *A&A*, 539, A137
- Metropolis, N., Rosenbluth, A. W., Rosenbluth, M. N., & Teller, A. H. 1953, *J. Chem. Phys.*, 21, 1087
- Morris, B. M., Mandell, A. M., & Deming, D. 2013, *ApJ*, 764, L22
- Nelder, J. A. & Mead, R. 1965, *Computer Journal*, 7, 308
- Patil, A., Huard, D., & Fonnesbeck, C. J. 2010, *Journal of Statistical Software*, 35, 1
- Perna, R., Heng, K., & Pont, F. 2012, *ApJ*, 751, 59
- Pont, F., Knutson, H., Gilliland, R. L., Moutou, C., & Charbonneau, D. 2008, *MNRAS*, 385, 109
- Pont, F., Sing, D. K., Gibson, N., Aigrain, S., Henry, G., & Husnoo, N. 2013, *MNRAS*, in press
- Rowe, J. F., Matthews, J. M., Seager, S., Miller-Ricci, E., Sasselov, D., Kuschnig, R., Guenther, D. B., Moffat, A. F. J., Rucinski, S. M., Walker, G. A. H., & Weiss, W. W. 2008, *ApJ*, 689, 1345
- Seager, S. 2010, *Exoplanet Atmospheres: Physical Processes* (Princeton: Princeton Univ. Press)
- Showman, A. P., Fortney, J. J., Lian, Y., Marley, M. S., Freedman, R. S., Knutson, H. A., & Charbonneau, D. 2009, *ApJ*, 699, 564
- Sing, D. K., Désert, J.-M., Lecavelier Des Etangs, A., Ballester, G. E., Vidal-Madjar, A., Parmentier, V., Hebrard, G., & Henry, G. W. 2009, *A&A*, 505, 891
- Sing, D. K., Pont, F., Aigrain, S., Charbonneau, D., Désert, J.-M., Gibson, N., Gilliland, R., Hayek, W., Henry, G., Knutson, H., Lecavelier Des Etangs, A., Mazeh, T., & Shporer, A. 2011, *MNRAS*, 416, 1443
- Snellen, I. A. G., de Mooij, E. J. W., & Albrecht, S. 2009, *Nature*, 459, 543
- Snellen, I. A. G., de Mooij, E. J. W., & Burrows, A. 2010, *A&A*, 513, A76
- Sudarsky, D., Burrows, A., & Pinto, P. 2000, *ApJ*, 538, 885

Welsh, W. F., Orosz, J. A., Seager, S., Fortney, J. J., Jenkins, J., Rowe, J. F., Koch, D., & Borucki, W. J. 2010, *ApJ*, 713, L145